Materials Today Bio 30 (2025) 101433

Contents lists available at ScienceDirect

Materials Today Bio

journal homepage: www.journals.elsevier.com/materials-today-bio

Melanoma extracellular vesicles membrane coated nanoparticles as targeted delivery carriers for tumor and lungs

María Sancho-Albero [a,**,1], Alessandra Decio [b], Reha Akpinar [c,d], Ada De Luigi [a], Raffaella Giavazzi [b], Luigi M. Terracciano [c,d], Luisa De Cola [a,e,*]

[a] Department of Biochemistry and Molecular Pharmacology. Istituto di Ricerche Farmacologiche Mario Negri, IRCCS, Via Mario Negri, 2, Milan, Italy
[b] Department of Oncology. Istituto di Ricerche Farmacologiche Mario Negri, IRCCS, Via Mario Negri, 2, Milan, Italy
[c] IRCCS Humanitas Research Hospital, via Manzoni 56, Rozzano, 20089, Milan, Italy
[d] Department of Biomedical Sciences, Humanitas University, Via Rita Levi Montalcini 4, Pieve Emanuele, 20072, Milan, Italy
[e] Department of Pharmaceutical Science, DISFARM. Università degli Studi di Milano, Milan, 20133, Italy

A B S T R A C T

Targeting is the most challenging problem to solve for drug delivery systems. Despite the use of targeting units such as antibodies, peptides and proteins to increase their penetration in tumors the amount of therapeutics that reach the target is very small, even with the use of nanoparticles (NPs). Nature has solved the selectivity problem using a combination of proteins and lipids that are exposed on the cell membranes and are able to recognize specific tissues as demonstrated by cancer metastasis. Extracellular vesicles (EVs) have a similar ability in target only certain organs or to return to their original cells, showing home behavior. Here we report a strategy inspired by nature, using a combination of NPs and the targeting cell membranes of EVs. We implement the EV membranes, extracted by the EVs produced by melanoma B16-BL6 cells, as a coating of organosilica porous particles with the aim of targeting tumors and lung metastasis, while avoiding systemic effects and accumulation of the NPs in undesired organs. The tissue-specific fingerprint provided by the EVs-derived membranes from melanoma cells provides preferential uptake into the tumor and selective targeting of lungs. The ability of the EVs hybrid systems to behave as the natural EVs was demonstrated *in vitro* and *in vivo* in two different tumor models. As a proof of concept, the loading and release of doxorubicin, was investigated and its accumulation demonstrated in the expected tissues.

1. Introduction

Being able to target a specific tissue or cell type is the holy grail of targeted therapies such as drug delivery. However, this is still extremely challenging both for small molecules and for nanoparticles (NPs) and as a consequence, many potential drugs do not find clinical applications [1]. Nature offers examples of selective targeting, being cancer metastasis a particularly striking one. Specific types of cancer metastasize selectively in determined organs showing the ability of cancer to recognize and target tissue-specific features. The mechanism of this tropism is under study but an increasing number of reports point out that extracellular vesicles (EVs) (including exosomes), as well as soluble factors released from primary tumor cells, induce the release of progenitor cells and their targeted migration to a specific future metastatic site. Mimicking nature is however very complex and simpler approaches have been reported in the attempt to have passive [2] and active [3] targeting especially when, using NPs, combinations of specific sizes, ligands, surface derivatization can promote a certain biodistribution.

A large variety of nanostructured materials have been developed with exciting therapeutic properties [4–7] but all the reported systems as lipid-based, polymeric and inorganic NPs are still far from efficient in reaching the desired sites and in particular to selectively target tumor microenvironment and cancer cells. Thousands of proof of concept papers using nanomaterials and drugs functionalized with a wide variety of different moieties (antibodies, peptides, aptamers, etc.) [8–11], have been reported being able to recognize specific molecules exposed by tumor cells, internalize, escape endosomes or exert their functions in the tumor microenvironment in response to internal or external signals.

* Corresponding author. Department of Biochemistry and Molecular Pharmacology. Istituto di Ricerche Farmacologiche Mario Negri, IRCCS, Via Mario Negri, 2, Milan, Italy.
** Corresponding author.
E-mail addresses: luisa.decola@marionegri.it, luisa.decola@unimi.it (L. De Cola).
[1] Instituto de Investigación Sanitaria de Aragón (IIS Aragón), Avda. San Juan Bosco, 13, 50009 Zaragoza, Spain; Instituto de Nanociencia y Materiales de Aragón (INMA), CSIC-Universidad de Zaragoza, Campus Rio Ebro, Edificio I+D, C/Poeta Mariano Esquillor, s/n, 50018 Zaragoza, Spain; Networking Research Center in Biomaterials, Bioengineering and Nanomedicine (CIBERBBN), Instituto de Salud Carlos III, 28029 Madrid, Spain and Department of Chemical and Enviromental Engineering, University of Zaragoza, Campus Rio Ebro, C/María de Luna, 3, 50018 Zaragoza, Spain.

https://doi.org/10.1016/j.mtbio.2024.101433
Received 21 October 2024; Received in revised form 17 December 2024; Accepted 27 December 2024
Available online 28 December 2024

Many of these exciting nano-formulations have been tested in clinical trials, close to 200 cancer nanomedicines were accounted for in the review by Schewndeman et al. [12] However, most of these promising advances have failed to materialize in the clinic even if some problems such as the circulation time of the therapeutic systems, their uptake from macrophages and the eventual toxicity or not complete elimination of the carriers have been somewhat overcome.

Amongst the materials used to construct the NPs, the liposomes [13,14] and lipidic structures [15] are the most investigated ones but also hard systems such as silica and organosilica [16,17] and porous silicon [18,19] have received great attention because of their size and shape tunability and porosity. They are also more stable in physiological condition than the soft counterparts and maintain the required properties to be used *in vivo* and become commercially interesting (e.g. high biocompatibility, degradability, large surface area for drug loading, easy storage, and low costs) [18–23]. Emerging strategy for enhancing efficiency of targeting, while avoiding the immune system recognition and improving NPs delivery to tumors have been also investigated [20,21]. Amongst them approaches combining the natural targeting behavior of EVs and therapeutics [22], or imaging nanomaterials are of great interest to target tumor sites with highly specific biodistribution and low immunogenicity [23–25]. The selective behavior of the EVs towards their mother cells (homing behavior) as well as the organs they naturally target [26], is certainly very appealing. EVs are nanovesicles (50–120 nm of diameter) from endocytic nature secreted by almost all cell types [27]. These EVs are formed by a cytosolic inner compartment where proteins, nucleic acids and biomolecules are located, and by a protein-phospholipidic double membrane.

Some authors have proposed the use of fruit-derived EVs as drug delivery platforms of doxorubicin (DOX) towards glioblastoma tumors, enhancing its antitumor efficacy *in vivo* (due to a highly penetration of the blood brain barrier, a deep penetration on glioblastoma and glioma tissues and an increased cellular internalization) [28,29]. Recently, citrus-isolated EVs have been also described as bioactive platforms to induce secondary necrosis and anti-tumor immunity in glioma cells improving immunochemotheray efficacy [30]. In other work, DOX-loaded lemon-derived EVs have been reported to overcome cancer multidrug resistance in ovarian cancer after being internalized mainly by caveolin-mediated endocytosis [31].

The high potential of EVs in targeting arises from the fact that cancer-derived EVs exhibit unique fingerprint properties associated to the specific composition of their membranes, maintaining the same homing tropism of the secreting parent cell lines. When these EVs are cancer cells or other cells with tumor tropism, such as stem cells, this feature can be exploited towards their preferential accumulation in cancer tissue and metastatic areas [22,32]

The described methodologies to encapsulate therapeutic molecules and NPs within EVs rely on sonication, extrusion or incubation with parental source cells. However, the use of the whole natural cancer-derived EVs presents one main limitation as they play a role in metastasis progression by promoting angiogenesis and creating new pre-metastatic niches [33]. To overcome this challenge, some authors reported the binding of NPs to the EVs surface or engineering the membrane of the vesicles to create new EVs-based nanoplatforms. For instance, it has been demonstrated how cancer cell membrane-camouflaged [34] or macrophage-derived membrane based [35] drugs delivery systems, significantly improved cell uptake (by tumor-targeting ability owning to its membrane coating) and enhanced cancer cell apoptosis. Also, in the last few years, other studies, proposed the use of biomimetic nanovesicle delivery systems to create fully artificial EVs-like particles to delivery mainly siRNA and miRNA against cancer [36–38].

Chernyshev et al., engineered multicompartment particles obtained from MCF7 and CHO cells and human plasma onto the surface of polyelectrolyte-coated silica particles. They demonstrated how the internalization of the silica particles was faster and more efficient when they were engineered with the vesicles, demonstrating how the vesicles provide the NPs with an exceptional interaction and adhesion properties with the target cells [39]. Zhou et al., created lipid-EVs hybrids by the fusion of tumor-derived EVs with phospholipids to create a delivery vector to tumors and a high efficient transfection agent of siRNA [40]. In this study, they used tumor-derived EVs membranes isolated from Sk-hep1 cells combined with phospholipids to create bioartificial vesicles that were electroporated in the presence of CDK1 siRNA. They demonstrated how the targeting properties of EVs membranes combined with the high loading siRNA efficacy of liposomes leading to a superior accumulation and internalization in cancer cells, *in vivo*, inhibiting tumor growth and prolonging the survival of tumor-bearing mice. Also, Wang et al. [41], have developed an acoustofluidic device that simultaneously achieved drug loading and EVs encapsulation. They created a drug-loaded silica nanocarrier that is encased within an EV membrane. These EVs-encapsulated nanocarriers exhibit excellent efficiency in intracellular transport and are capable of significantly inhibiting tumor cell proliferation [41]. In a different study, Li et al., used the upconversion (UC) NPs modified with mesoporous silica (SUC) to load an HDACI, suberoylanilide hydroxamic acid (SAHA), and further camouflaged with M1 macrophage-derived EVs membranes (EMS). In tumor-bearing mice, EMS showed spatiotemporal-resolved properties and facilitated the drug accumulation in the tumors, which induced superior anti-tumor effects [42]. Nevertheless, although during recent years cancer-derived EVs have been widely combined with nanomaterials and even with silica NPs, the use of the whole natural cancer derived vesicle present one main problem as they are also involved in facilitating tumor proliferation and metastasis dissemination, as well as immunogenicity and angiogenesis [33], limiting their translation to the clinic [43,44].

Herein we explore the possibility to create a targeting carrier based on EVs-derived phospholipid-protein-coated breakable organosilica porous particles, nanocages. Unlike most of the published studies that encapsulate the nanomaterials in the EVs, we have isolated the membrane (or large fragments) from the melanoma EVs to avoid the pro-oncogenic components of the EVs and reduce the immunoresponse *in vivo*. Our study demonstrates that NPs loaded covered with EVs membranes were accumulated in lungs and that, when loaded with therapeutic drugs, they can be a potential alternative for cancer treatment approaches. In a previous work, we demonstrated the successful use of organosilica nanocages (ssOSCs) as antitumoral drug delivery carriers [45]. We therefore maintained these small NPs (20 nm) and electrostatically covered them with the EVs membrane. A full characterization of the hybrid system revealed that the full coverage is realized when the size of the EVs membrane is 3 times bigger than the NPs employed and the interaction between the membrane and the nanomaterials is fully driven by a strong electrostatic attraction. We demonstrate the selectivity towards cancer cells *in vitro* and towards the tumor and the lungs in tumor-bearing mice (in a spontaneous and in an artificial lung metastases animal models).

2. Experimental part

2.1. Synthesis and characterization of organosilica nanocages

Cage-like breakable organosilica NPs were synthesized and characterized following a previously published protocol [46–49]. Cetyltrimethylammonium bromide (CTAB) was used as the template of the cage-like NPs and tetraethoxysilane (TEOS) and bis3-(triethoxysilyl) propyl]disulphide BTDS were employed for synthetizing the disulfide breakable organosilica framework. Then, NPs were positively functionalized in a one-pot synthetic approach before being coated with the EVs -derived membranes by adding (3-Aminopropyl) triethodysilane (APTES) to the NPs solution [46]. For the *in vitro* and the *in vivo* experiments, breakable organosilica nanocages (ssOSCs) were fluorescently labelled using sulfo-Cy5-NHS dye [46].

NPs size and morphology were evaluated by TEM (T20-FEI Tecnai thermoionic, TEM) operated at 200 kV with a LaB6 electron source fitted with a "SuperTwin®" objective lens allowing a point-to-point resolution of 2.4 A) using cupper grids. The hydrodynamic diameter and the surface charge of the ssOSCs and ssOSCs-NH_2 were characterized by DLS (Delsa Nano C Particle Analyzer (Beckman Coulter, operative wavelength 655 nm)). The presence of the disulfide bonds in the organosilica structure and the NH_2 functionalization groups on their surface was conducted by FTIR (Shimadzu IRAffinity-1 spectrometer). The attenuated total reflectance Fourier transform infrared (ATR-FTIR) spectra of the particle samples were collected using a spectral resolution of $\lambda = 4$ cm−1, accumulating 45 scans from 600 cm to 1 to 4000 cm-1.

2.2. Isolation and assembly of the cancer cell membrane fragments derived from EVs

B16-BL6 melanoma cells were provided by IJ Findler (Houston, TX), who originally establish and characterized this highly metastatic variant [50,51]. They were grown in a Minimum Essential Medium (MEM, Euroclone, Italy) supplemented with 10 % FBS (GIBCO, USA), 1 % penicillin/streptomycin (Biowest, France), 1 % L-glutamine (Euroclone, Italy), 1 % non-essential amino acids (Euroclone, Italy), 1 % sodium pyruvate (Euroclone, Italy) and 2 % of vitamin solution (Euroclone, Italy). NIH-3T3 cells (purchased from ATCC) were grown in Dulbecco's modified Eagle's medium (DMEM, Biowest, France) supplemented with 10 % fetal bovine serum (FBS, GIBCO, USA), 1 % penicillin/streptomycin (Biowest, France). Both cell lines were maintained at 37 °C in a 5 % CO_2-humidified atmosphere under normoxic conditions.

The culture media free of EVs was obtained by depleting the EVs from the serum by ultracentrifugation 100000 g for 8 h at 4 °C.

B16-BL6 derived EVs ($EVs^{B16-BL6}$) and NIH-3T3-derived EVs ($EVs^{NIH-3T3}$) were purified following an ultracentrifugation protocol [52]. Firstly, cells were seeded and incubated with cell culture media free of EVs for 48 h. Then, their supernatants were collected and were centrifuged during 20 min at 2000 g at 4 °C. Afterward, samples were centrifuged for 30 min at 10000 g and at 4 °C for discarding the microvesicles. To finally isolate the EVs, samples were ultracentrifuged for 2 h at 100000 g at 4 °C. The EVs pellet was washed by being resuspended in PBS and ultracentrifuged again for 2 h at 100000 g at 4 °C. The final precipitates were suspended in PBS and their concentration was calculated in terms of total protein amount by Pierce protein BCA assay (Thermo-Fisher Scientific, USA).

Before purifying their membranes, $EVs^{B16-BL6}$ were accurately characterized by a battery of physico-chemical and biological techniques. Western blot analysis was performed to determine the specific EVs surface proteins. Briefly, 20 μg of EVs (obtained by BCA and expressed as total protein amount) were suspended in Laemmli buffer and incubated at 95 °C during 10 min. Then, proteins were subsequently separated in a 12 % SDS-PAGE gel at 60 mV during the first 30 min and then at 120 mV (2 h). Subsequently, they were transferred to a polyvinylidene fluoride membrane (Immobilon-P PVDF, Millipore). Blots were blocked during 1 h with non-fat milk buffer (5 % in TBS, 0.1 % Tween-20, Fluka*)* at room temperature. Finally, they were incubated with the EVs antibodies: CD81 (mouse monoclonal (B-11), 1:1000, Santa Cruz Biotechnology), ALIX (mouse anti-Alix Monoclonal Antibody (3A9), 1/1000, Invitrogen), CD63 (rabbit monoclonal (EPR21151), 1:2500, Abcam) and β actin (mouse monoclonal (C4), 1:2000, Merck Life Science). Membranes were washed three times with TBS-Tween-20 (0.1 %) during 30 min followed by incubation of the secondary antibody (goat-anti-mouse IgG-Peroxidase (1/5000), Merck Life Science), and goat-anti-rabbit IgG-Peroxidase (1/5000), Merck Life Science). Before being imaged by chemiluminescence, they were washed three times again. DLS analysis was carried out to determine the diameter and zeta potential to estimate the surface charge of the isolated EVs. TEM and CryoTEM (LMA from University of Zaragoza) were employed for determine the morphology of the vesicles. Phosphotungstic acid (3 %) was used as negative contrast agent to stain the EVs. The membranes of EVs were extracted by using a modified Folch extraction protocol [53]. In brief, EVs suspensions were re-suspended in a mixture of CHCl3: MeOH (2:1 v/v). Samples were then vigorously vortexed at room temperature during 10 min, and they were finally centrifuged at 6000 g for 10 min. After the centrifugation, a biphasic mixture separated an interface was formed and the bottom part (containing the isolated hydrophobic EVs components) was extracted with a glass pipette. Samples were completely dried with nitrogen atmosphere and storage at −20 °C until use. Then, the ssOSCs covered with the membranes were prepared by thin film hydration. Briefly, the obtained dried membranes films were hydrated by adding the ssOSCs aqueous dispersion to allow their adsorption on the silica NPs (ratio $EVs^{B16-BL6}$/ssOSCs 1:3 w/w). Then, the mixture was sonicated for 20 min to obtain the EVs membrane-covered ssOSCs. Diverse ratios $EVs^{B16-BL6}$:NPs were tested in order to optimize their coupling. In particular, besides the selected 1:3 ratio, 1:0.1; 1:0,5; 1:1; 1:3, 1:10 and 1:50 w/w were tested to evaluate the best condition to obtain a 1 nanocage per EVs membrane. The EVs membrane coated ssOSCs were thoroughly characterized in terms of DLS, zeta potential, TEM, and CryoTEM as previously described. Also, fluorescence polarization and co-localization experiments by confocal microscopy. Membrane microviscosity was assessed in cell suspension using 1,6-diphenyl-1,3,5-hexatriene (DPH) as a fluorescence probe [54]. The reported fluorescence polarization (p) value is a function of the emission (420 nm), detected through an analyzer oriented parallel and perpendicular to the direction of the polarization of the exciting light (365 nm) according to an equation previously reported [54]. For the fluorescence polarization measurements, a DPH solution prepared by diluting 1:1000 in PBS a stock DPH solution (2 mM in tetrahydrofuorane). Ten μL of this solution were added to the samples before measuring their polarized fluorescence in a TECAN Infinite F500 plate reader (λex = 365 (25) nm and λem = 430 (20) nm). To finally prove the correct formation of the EVs -derived membrane layer around the silica nanocages, fluorescence microscopy colocalization assays were performed. In particular Cy5 labelled NPs were used. EVs membranes, after NPs coating, were labelled with DiO (DiO (DiOC18(3) (3,3′-dioctadecyloxacarbocyanine perchlorate)) from Thermo-Fisher Scientific, adding 0.5 μL of 10 μg mL−1 DiO solution in DMSO for each mg of lipid-coated nanocages. The nanoconstructs were then incubated at 37 °C for 30 min in shaking mode (200 rpm). After the incubation, 5 μL of lipid-coated nanocage dispersion was deposited on a glass slide, coated by a cover glass slip and analyzed through a confocal microscope (Nikon A1 confocal scan unit with a 100 × 1.49 NA oil immersion objective managed by NIS elements software). To again prove the EVs membrane coating around the NPs, FTIR analysis was also performed as previously mentioned. SDS-gel stained with Coomassie (brilliant blue R250, 0.25 % in 45 % methanol + 10 % glacial acetic acid, Sigma Aldrich) and TLC experiments were carried out to examined their proteomic and lipidomic content, respectively. TLC experiments were carried out following a previous published protocol with slight modifications [55]. Briefly, silica gel TLC (20 × 20 cm) were prewashed in chloroform-methanol 2:1 (v/v) before being used. After sample etching the plate was dipped in methanol-water 50:50 (v/v) and activated at 100 °C for 45 h in vacuum oven. Then, lipids were separated using chloroform-methanol-acetic acid-water 50:30:8:4 (v/v/v/v). The developed plate was dried by heating at 100 °C for 5 min. To stain the lipids, the plate was placed for few minutes in an iodine chamber. Finally, ssOSCs were also covered with EVs fragments isolated from NIH-3T3 (ssOSCs-$EVs^{NIH-3T3}$) following the protocol described above. These cells are the healthy counterpart of B16 cell line [56–58] and where used in the *in vitro* internalization experiments as control-covered EVs.

2.3. Selective in vitro cell uptake of EVs-covered NPs by confocal microscopy and flow cytometry

The selectiveness in the internalization process of the ssOSCs-EVs$^{B16-BL6}$, was evaluated in B16-BL6 cell cultures and in NIH-3T3 cells by confocal microscopy and by flow cytometry. The uptake kinetics of ssOCS-EVs$^{NIH-3T3}$ was also studied. Firstly, confocal experiments were carried out. Both B16-BL6 (tumoral) and NIH-3T3 (healthy) cells were seeded at a density of 4×10^4 cells/well onto 20 mm coverslips placed in 24-multi well plates and allowed to growth during 24 h. In order to visualize the hybrid EV-based NPs, their phospholipid membrane was labelled with the fluorescent dyes PKH-26 (red) and PKH-67 (green) following the manufacturer recommendations and previously published protocols [59]. Then, the fluorescent labelled ssOSCs-EVs$^{B16-BL6}$ and ssOSCs-EVs$^{NIH-3T3}$ (0.1 mg mL−1) were resuspended in cell culture media and were simultaneously added to the cells during 2, 4, 8, 12, 24, and 48 h. In the case of the B16-BL6 cell cultures, ssOSCs-EVs$^{B16-BL6}$ and ssOSCs-EVs$^{NIH-3T3}$ were labelled with the green PKH-67 dye and red fluorescent the PKH-26, respectively. On the contrary, when incubating the vectors with the healthy NIH-3T3 cells, ssOSCs-EVs$^{B16-BL6}$ were labelled in red and ssOSCs-EVs$^{NIH-3T3}$ in green. Afterward, cells were fixed with paraformaldehyde (PFA) 4 % during 20 min and washed three times with PBS. Hoechst 33342 was used to observe the nuclei. Finally, the cellular uptake was determined by confocal microscopy (Nikon A1 confocal scan unit with a 100 × 1.49 NA oil immersion objective managed by NIS elements software).

The capacity of EVs-based vectors of being selectively internalized was also assessed by flow cytometry. Briefly, 4×10^4 cells were seeded onto a 24-well plate. Then, ssOSCs-EVs EVs$^{B16-BL6}$ and ssOSCs-EVs$^{NIH-3T3}$ (0.1 mg mL-1) were added separately in different cell wells and incubated with tumoral B16-BL6 and with healthy NIH-3T3 cell cultures. In these flow cytometry experiments, all the EVs-based vectors were always labelled with the same probe (PKH-67) in order to discard any possible effect of the dye in the cell uptake kinetics. At specific time points (2, 4, 8, 24, 48, and 72 h after the treatment), cells were collected and analyzed by flow cytometry using Cytoflex LX instrument (Beckman coulter), and the data were analyzed by Kaluza Software (Beckman Coulter). Non-treated cells were used to set the gate and the percentage of positive cells to assess NPs internalization. For the detection of PKH-67 labelled ssOSCs-EVs excitation wavelength of 488 nm was used. All the samples were analyzed acquiring at least 10000 events.

2.4. Drug loading experiments

DOX was encapsulated into the ssOSCs following a conventional impregnation and previously published protocol [46]. The encapsulation of the drug was performed before their functionalization with the APTES. Briefly, 20 mg of naked ssOSCS were suspended in 5 mL of EtOH and 20 mg of DOX (Sigma Aldrich) were dissolved in 5 mL of the same solvent and sonicated for 10 min separately. Subsequently, they were mixed and sonicated for 20 additional min and stirred for 12 h at room temperature and in darkness. The day after, and to force the encapsulation of the therapeutic molecule in the internal cavity of the nanocages, the solvent was eliminated under high vacuum. Then, the loaded NPs were washed with water five times to eliminate the non-encapsulated drug. Finally, and before the covering with the EVs membrane, the NPs were positively functionalized. Particularly, they resuspended in toluene (2 mL), 150 μL of 2,2-dimethoxy-1,6-diaza-2-silacyclooctane and 1 μL of NH4OH (28 %) were added and the solution was left for 12 h in continuous agitation at room temperature. The positive NPs were washed three times with water and stored at 4 °C until further use. As the empty NPs, the loaded ssOSCs were thoroughly characterized by TEM, DLS, zeta potential, FTIR and emission spectroscopy (λex = 470 nm).

2.5. Animal and tumor models optimization

Studies were conducted in conformity with the institutional guidelines that comply with national (Legislative Degree 26/2014) and international (Directive 2010/63/EU) laws and policies, in line with the guidelines for the welfare and use of animals in cancer research. They were approved by the Mario Negri Institute Animal Care and Use Committee (IACUC) and authorized by the Italian Ministry of Health, Directorate General for Animal Health and Veterinary Medicines (Authorization No. 736/2022-PR).

For these experiments 6-8-week-old female C57BL/6 mice (Charles River, Italy) were employed. Animals were maintained under 7 days quarantine before starting the experiments and tumor cells were maintained in their media without antibiotic for 24 h before injection. For the subcutaneous model, mice received an injection of $2x10^5$ B16-BL6 cells suspended in 200 mL of Hanks' Balanced Salts Solution (Euroclone, Italy) and tumor size, representative of tumor growth, was measured with a caliper twice a week. For the artificial metastasis model, $5x10^4$ B16-BL6_Luc cells (stable infected with the luciferase reporter gene) were intravenously injected to the mice in the tail vein. The progression of the B16BL6_Luc cells in the lung was evaluated by bioluminescence imaging (IVIS Lumina XRMS Series III, Perkin Elmer) after the injection of 150 mg kg-1 of D-luciferin (Perkin Elmer, Italy), as previously described. At sacrifice, lungs were removed, fixed in formalin and the metastatic burden was assessed by counting the metastasis nodules. To evaluate the potential weight loss during the experiments, mice were weighted every two days. The experimental plan containing the time points, the analysis and the sampling is included in Fig. S1.

2.6. Biodistribution and therapy efficacy studies

In the biodistribution studies, after tumor implantation mice were randomly divided in groups by tumor dimensions. Each group represents a different time point of sacrifice for every type of organosilica nanocages administered. 7 mg kg-1 of ssOSCs and ssOSCs-EVs$^{B16-BL6}$ were administered in the tail vein and due to their fluorescence with the Cy5 dye attached to the silica core, their presence in the mice was visualized 4, 24, 48 h and 1 week after administration under an IVIS equipment (IVIS Lumina XRMS Series III). Tumor, kidneys, liver, lungs, spleen and pancreas were collected from each animal for histopathological analysis (described below) and to evaluate the Si bioaccumulation by Inductively Coupled Plasma Optical Emission Spectroscopy (ICP-OES). To quantify the amount of Si, each organ was digested with 3 mL of nitric acid during 5 days at room temperature. The samples were filtered with a 0.2 syringe filter and diluted in 1/10 in miliQ H2O and total amount of Si element within the tissues was determined by ICP-OES (Thermo Scientific I CAP PRO XP Duo) in the Chemical Analysis Service from the University of Zaragoza. To determine the relevance of the EVs-based vectors a proof of concept of their therapeutic efficacy was assessed in both the subcutaneous tumor growth and the artificial metastasis models. For each cancer model, mice were divided in four groups intravenously administered: PBS (group 1), free DOX (7 mg kg-1) (group 2), empty ssOSCs-EVs$^{B16-BL6}$ (group 3) and DOX (equivalent dose of group 2)-loaded ssOSCs-EVs$^{B16-BL6}$ (group 4).

For the subcutaneous model, treatments started when the primary tumor reached approx. 0.5 cm^3 and repeated 5 and 10 days after the first administration. Tumor size was measured twice weekly using a caliper. In the metastatic model, treatment started 13 days after tumor cell injection and repeated every 5 days for three administrations. The presence of tumor in lungs was monitored by bioluminescence (using IVIS Lumina) at days 12, 21 and 27 after tumor implantation. The number and size of metastasis in the lungs were determined at the end-point of the experiment.

Two different and independent experiments were carried out in order to evaluate the biodistribution and tolerability of the ssOSCs and the ssOSCs-EVs$^{B16-BL6}$ and to assess the efficiency of the DOX-loaded

ssOSCS-EVs$^{B16-BL6}$.

2.7. Histopathological studies

After the euthanasia of the animals, tumor, kidneys, liver, lungs, spleen and pancreas were collected. Samples were fixed in formalin for 24 h, followed by 70 % ethanol. Tissue samples were then embedded in paraffin and 5 μm sections were stained with hematoxylin and eosin (HE).

In the biodistribution studies, the presence of the vectors in the different tissues was evaluated by the presence of the fluorescence NPs within the different tissues carrying out an immunofluorescence analysis by fluorescence microscopy. Samples were frozen with isopentane cooled by liquid nitrogen and cryo-sectioned at 5 μm. Slices were assembled in a slide with FluoromontG and DAPI (λex/em 364/454) for visualization under the virtual microscope (Olympus BX61VS Microscope) using a 20x objective.

In the antitumoral activity experiments, tumor cell proliferation was evaluated by Ki-67 expression (Thermofisher, clone SP6). Along with the antibody BOND-III Automated IHC Stainer (Leica Biosystems) was employed for sections (4–5 μm).

Samples were visualized under a virtual microscopy (Olympus BX61VS Microscope). HE slides of organs were evaluated for the presence of malignancy and other non-neoplastic features. Ki-67 proliferation index was calculated through the counting of the percentage of positive cells present in three distinct and random areas within the mice tumors from every group.

2.8. Statistical analysis

All the results are expressed as mean ± SD. Statistical analysis of the data and the significant differences among the means were analyzed by one way and two-way analysis of variance (ANOVA) for multiple comparisons by Dunnett's multiple comparisons test (GraphPad Software). Statistically significant differences were expressed as follows Mean ± sd. *p < 0.05; **p < 0.01; ***p < 0.0001 y ****p < 0.00001.

3. Results and discussion

3.1. Characterization of organosilica nanocages and assembly of the cancer cell membrane fragments derived from EVs

As mentioned above the porous materials used in this work are organosilica nanocages (ssOSCs) able to break on demand and in particular, when they are internalized in tumor cells. In fact, the presence of disulfide (S-S) groups in the silica network, allows the particles to disintegrate when a reducing agent, such as glutathione, reduces the disulfide to thiols. ssOSCs were synthesized and positively functionalized with APTES following a sol-gel template preparation protocol previously reported [46]. The amino-propyl groups on the surface of the silica NPs promote their coupling with EVs membranes by electrostatic interactions, since the primary amines are protonated at physiological pH and the EVs membranes are negatively charged. The morphology, size and functionalization of the obtained NPs was assessed by a variety of techniques.

Fig. 1A shows TEM images where the typical cage-like structure of the NPs is clearly visible. These NPs exhibited a diameter around 18 nm, in agreement with the hydrodynamic diameter of 20 nm, evaluated by DLS (Fig. 1B) and a zeta potential ζ = −13.9 ± 2.1 mV. After the functionalization with the amino-propyl groups, the NPs exhibited a ζ of +33.6 ± 1.3 mV. The functionalization of the ssOSCs' surface was also confirmed by FTIR (Fig. 1C). The spectrum confirms the characteristic fingerprint of the organosilica structure (green): Si–OH (3445 cm−1), Si–O–Si (1077 cm−1) Si–OH (947 cm−1) and C–H (805 cm−1). Also, the methylene groups coming from the breakable disulfide linker present in the NPs were observed at 2927-2868 cm-1 bands (yellow).

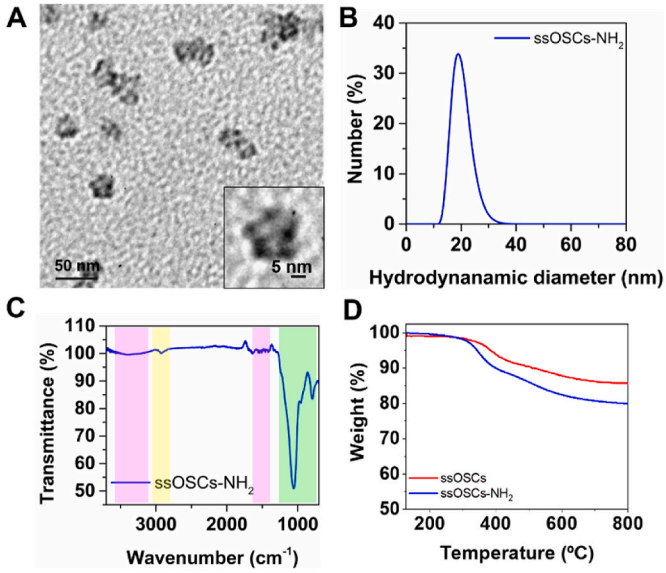

Fig. 1. ssOSCs-NH_2 characterization. A) TEM images. In the insert the characteristic cage-like form with the single internal pore is observed. B) DLS analysis. C) FTIR spectrum containing the characteristic peaks of the silica framework (green), disulfide organic groups in the silica structure (yellow) and the NH_2 on the NPs surface (pink). D) TGA of ssOSCs-NH_2 and comparison with the naked ssOSCs. (For interpretation of the references to colour in this figure legend, the reader is referred to the Web version of this article.)

Finally, the peaks of the amino silane molecule anchored on the surface of the NPs were observed (pink): 3378 and 1416 cm−1. To quantify the amount of amino groups on the ssOSCs-NH_2 the TGA analysis was performed, Fig. 1D, confirming the presence of the breakable disulfide groups introduced into the silica structure (corresponding to 10–15 % of sample mass) and the functionalization with the NH_2 groups (10 % in weight). These results were in agreement with previous published work [46].

EVs were isolated from the melanoma cancer B16-BL6 cells (EVs B16-BL6) and from healthy murine fibroblasts NIH-3T3 (EVs NIH-3T3) cell lines and characterized, before the extraction of their membranes, by different procedures, including physicochemical (TEM, DLS and zeta potential) and biological (Western blot assays against different protein markers and total protein content) techniques. Fig. 2A and Fig. S2A containing TEM images of the isolated EVs B16-BL6 confirming the presence of spherical vesicles with an average diameter around 70 nm. DLS analysis corroborate the results, revealing a hydrodynamic diameter of 80 nm (Fig. 2B) in PBS and a zeta potential of ζ = -14.6 ± 4.7 mV, due to the negatively charged phospholipids present on the EVs membrane. Isolated EVs NIH-3T3 TEM images also show spherical shaped vesicles, corresponding to the EVs with an average size around 100 nm (Fig. 2C and Fig. S2B). DLS analysis gave a mean particle diameter of 144 nm in PBS (Fig. 2D). The measured surface charge of EVs$^{NIH-3T3}$ was ζ = -12.1 ± 3.5 mV. To further confirm that the isolated particles are indeed EVs, the presence of EVs-specific marker proteins (ALIX, CD81 and CD63) were characterized by western blot (Fig. 2E). ALIX, CD81 and CD63 proteins are specifically expressed only in EVs$^{B16-BL6}$ and EVs$^{NIH-3T3}$ compared to the macrovesicles and the cell lysates.

As already mentioned, most of the published work rely on the use of the EVs or biomimetic systems to enhance the targeting properties. In our approach, we have chosen to use only the EV membranes, obtained from the melanoma cancer cell lines, to assure the homing tropism towards the cancer cells as well as the targeting of the lungs as the natural melanoma cells. The EVs membrane will then be used as a coating for nanocarriers filled with drugs or even fragile molecules, to avoid leakage during the circulation and degradation in complex fluids. The size, monodispersity and breakability and elimination of our nanocages make

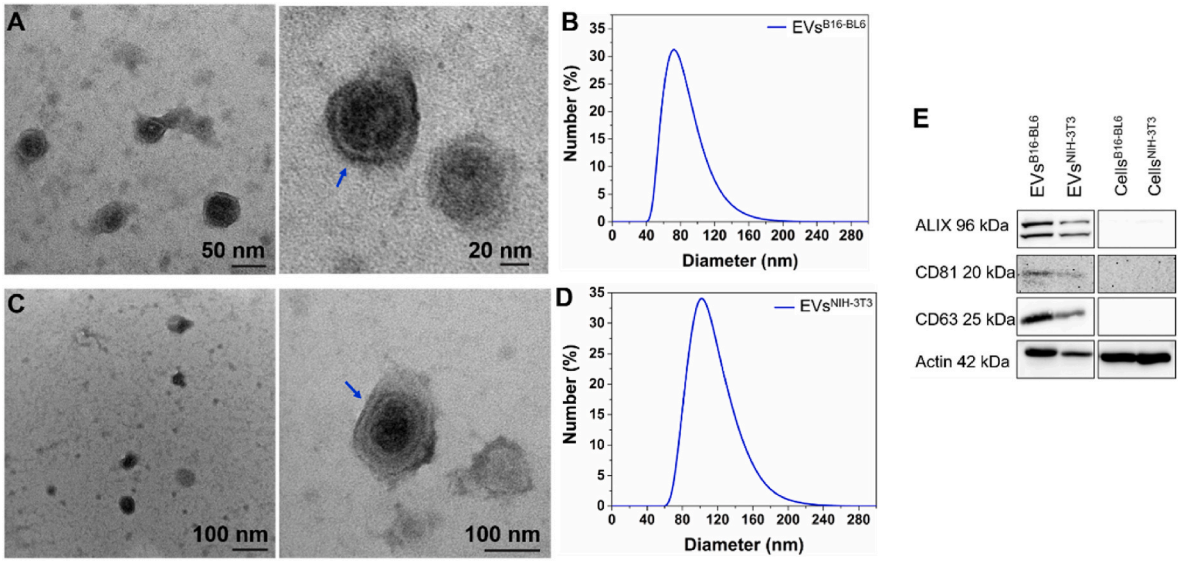

Fig. 2. EVs characterization. A) Representative TEM images of $EVs^{B16-BL6}$ (stained with PTA 3 %) at different magnifications. Blue arrows indicate the presence of the characteristic lipidic membrane of the EVs. B) DLS analysis of $EVs^{B16-BL6}$. C) Representative TEM images of $EVs^{NIH-3T3}$ at different magnifications. D) DLS analysis of $EVs^{NIH-3T3}$. E) Western blot evaluation of one representative isolation of EVs (ALIX, CD81, CD63) and control (actin) proteins for $EVs^{B16-BL6}$ and $EVs^{NIH-3T3}$. The expression of these proteins in microvesicles and in cells pellets collected during the ultracentrifugation cycles were used as control. (For interpretation of the references to colour in this figure legend, the reader is referred to the Web version of this article.)

these nanocarriers ideal candidates to be covered with the EVs membranes.

To optimize the NPs coverage, and to avoid having empty EVs or multiple ssOSCs inside the same EVs we tested different ratio in weight (μg) of $EVs^{B16-BL6}$-derived membranes vs ssOSCs. In particular the amount of membranes was kept constant (100 μg) and the NPs mass was varied from 10 to 5000 μg (Table S1). The NPs coating was evaluated by measuring the hydrodynamic diameter by DLS (Fig. S3A) and assuring the complete coverage with the negatively charged membrane by the change of the zeta potential (Fig. S3B). In all the ratios tested, the hydrodynamic diameter of all the samples was always around 100 nm but at higher ratios, smaller diameters were also observed, suggesting the formation of vesicles from the membranes. Monitoring the zeta potential, the values obtained indicate that at the lowest concentration, a large number of EVs are empty while when increasing the amount of positively charge ssOSCs, the zeta potential of the adducted tend to be

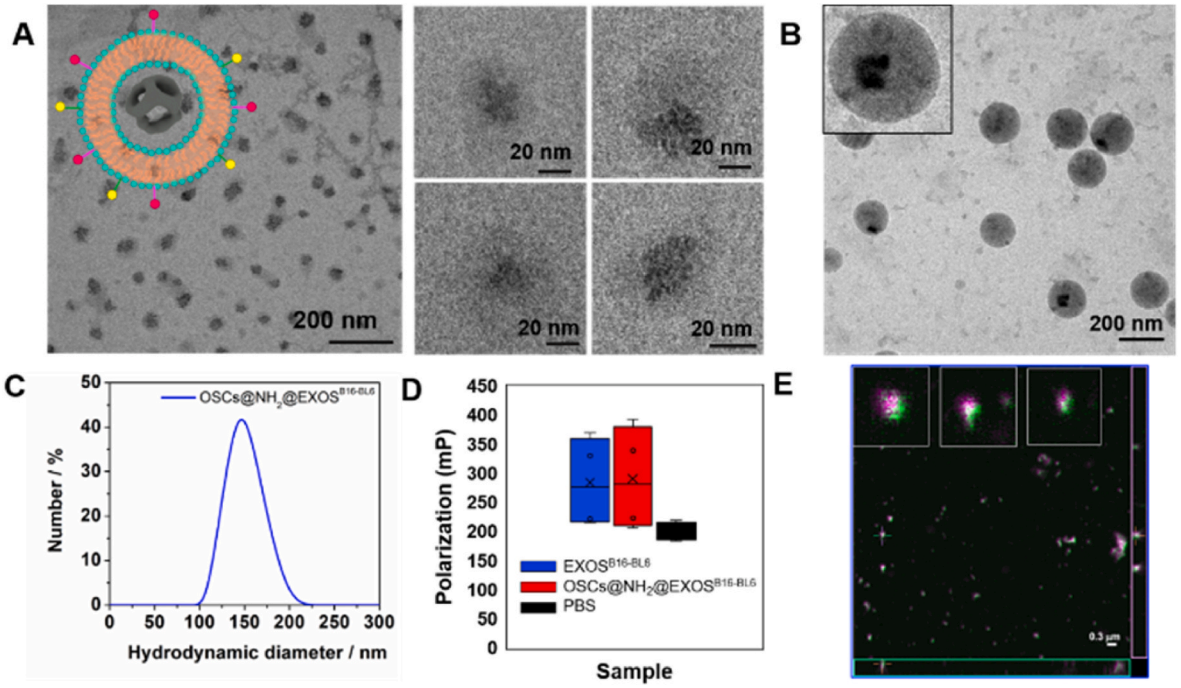

Fig. 3. Characterization of ssOSCs-$EVs^{B16-BL6}$. A) TEM analysis of the samples stained with PTA 3 %. In the zoom images, the core-shell structure can be observed. B) CryoTEM images evidencing the formation of the lipidic structures around the ssOSCs located inside them. C) Hydrodynamic diameter of the vesicles analyzed by DLS. D) Degree of fluorescent polarization of DPH-labelled samples (correlation with membrane lipid fluidity and microviscosity). E) Co-localization experiments carried out by fluorescence confocal microscopy (pink: ssOSCs and green: $EVs^{B16-BL6}$-derived membranes). (For interpretation of the references to colour in this figure legend, the reader is referred to the Web version of this article.)

less negative, evidencing that the NPs were probably not totally covered for a ratio above 1:5. The ratio 1:3 was chosen as the optimum $EVs^{B16-BL6}$ membranes: ssOSCs-NH_2 (w/w) ratio for performing the following *in vivo* and *in vitro* experiments.

The obtained cages covered with EVs membranes, ssOSCs-$EVs^{B16-BL6}$, were thoroughly characterized in terms of morphology, size distribution, zeta potential, microviscosity and lipid and protein membrane content. TEM (Fig. 3A) and CryoTEM (Fig. 3B) images of ssOSCs-$EVs^{B16-BL6}$ revealed NPs of pseudospherical shape composed by 1) a core of 20 nm of diameter (corresponding with the ssOSCs) and 2) an organic shell coming from the EVs membranes (of approximately 100 nm in diameter). DLS results (Fig. 3C) showed similar particle size distribution is about 120 nm of diameter for the ssOSCs-$EVs^{B16-BL6}$. Zeta potential measurements ($\zeta = -27.2$ mV) evidenced the covering of the positively charged ssOSCs-NH_2 with the $EVs^{B16-BL6}$ (highly negative due to the presence of the phospholipids). To evaluate the eventual change in viscosity due to the hard core fluorescence polarization measurements of $EVs^{B16-BL6}$ and ssOSCs-EVs,B16-BL6 where performed. These measurements, Fig. 3D, provide an index of microviscosity of the hybrid materials [60]. The results indicate that the ssOSCs-$EVs^{B16-BL6}$ exhibited a similar fluidity and microviscosity of the natural $EVs^{B16-BL6}$. To further evaluate the percentage of the fully covered NPs with the EVs-derived membranes, a fluorescence colocalization assay was performed. In brief, ssOSCs-NH_2 were covalently labelled with a red fluorescent cyanine (Cy5) dye ($\lambda ex = 633$ nm) through the reaction between the sulfo-Cy5-NHS derivative and the amino groups grafted on the nanocages. Independently, the EVs-derived membranes were labelled with DiO, a lipophilic dye, that displays green emission ($\lambda ex = 488$ nm). Using a confocal microscope, although the resolution limit dictated by Abbe's law does not permit to resolve the core-shell structure, the observation of the white emissive spots, due to the superimposition of the red and green emissions, collected from the two channels suggest the co-localization of the membranes with the nanocages. In Fig. 3E it is clearly visible that the assembled ssOSCs-$EVs^{B16-BL6}$ are the predominant species.

To determine the colloidal stability of the ssOSCs-$EVs^{B16-BL6}$, the particles were stored at room temperature up to 1 week. At each time point, particle size and zeta potential were measured by DLS (Figure S4A and Figure S4B, respectively). The particles do not exhibit any variation of their hydrodynamic size and any fluctuation of the surface charge, confirming their stability over 1 week. Once the ssOSCs-$EVs^{B16-BL6}$ were also the properties of the healthy ssOSCs-$EVs^{NIH-3T3}$ counterparts were evaluated. The hydrodynamic diameter, surface charge and stability of ssOSCs-$EVs^{NIH-3T3}$ are shown in Fig. S5.

The proteins anchored to the ssOSCs surface were characterized by gel electrophoresis. Fig. S6A includes an image of the acrylamide/bis-acrylamide gel electrophoresis of the naked ssOSCs, the coated ones and the EVs-derived membranes. For this analysis, ssOSCs were fluorescently labelled with Cy5 as mentioned above. As it can be observed, ssOSCs, ssOSCs-$EVs^{B16-BL6}$ and ssOSCs-$EVs^{NIH-3T3}$ remained trapped in the injection well position without entering in the gel. On the other hand, Fig. S6B shows a Coomassie staining of the gel of Fig. S6A. In this case, ssOSCs-$EVs^{B16-BL6}$ and ssOSCs-$EVs^{NIH-3T3}$ were positively stained with the Coomassie evidencing the presence of the proteins retained in the well were the NPs were also observed (red rectangle). On the contrary, in the case of the naked ssOSCs, no proteins were observed. In the wells with free EVs-derived membranes, free proteins migrated among the gel (blue rectangle). These findings demonstrate again the proper anchoring of the EVs-derived membranes to the surface of the NPs. Also, both ssOSCs-$EVs^{B16-BL6}$ and ssOSCs-$EVs^{NIH-3T3}$ exhibit the same polarity properties of the isolated membranes isolated from the EVs (Fig. S6C). The membrane coating was finally investigated by FTIR. Fig. S6D shows the FTIR spectra of the ssOSCs-$EVs^{B16-BL6}$ were besides the characteristic silica bands (previously described), the phospholipid fingerprinted peaks at 1765-1720 cm-1 (C=O), 1200-1145 cm-1 and 830-740 cm-1 (PO_2), 1145-970 cm-1 (P-O-C), 1200-970 cm-1 (P-O-C + PO_2 and 2926-2855 cm-1 (CH_2) were present.

3.2. Selectivity in vitro of cancer cell uptake of EVs-covered NPs

Once the EVs-based artificial NPs were synthetized and characterized, their preferential internalization in target cells was evaluated *in vitro*. Confocal microscopy and flow cytometry were employed to evaluate if the targeting properties and selectivity toward specific cells are reached by the use of the membranes coming from the cancer cells' EVs reconstructed on the ssOSCs surface. In Fig. 4A and Fig. S7A a comparison between the internalization, in melanoma B16-BL6 cells, of the two nanoparticles covered with the $EVs^{B16-BL6}$ and $EVs^{NIH-3T3}$, respectively. In particular, the cancer cells were co-incubated with ssOSCs-$EVs^{B16-BL6}$ (0.1 mg mL-1, labelled with a green emitter) and with ssOSCs-$EVs^{NIH-3T3}$ (0.1 mg mL-1, labelled with a red emitting dye) for 2, 4, 8, 12, 24 and 48 h. We observed that when ssOSCs covered with the cancer derived EVs membranes their internalization occurs preferentially in their parental cells, showing the homing effect typical for exosomes. As a control, the same experiments were performed with cell cultures of healthy fibroblasts NIH-3T3 (Fig. 4B and Fig. S7B). In this case, ssOSCs-$EVs^{B16-BL6}$ were labelled in red (0.1 mg mL-1) and ssOSCs-$EVs^{NIH-3T3}$ (0.1 mg mL-1) were marked in green. In this case, and in particular at the higher tested-time points, yellow pixels were observed inside the cells meaning that ssOSCs-$EVs^{NIH-3T3}$ and ssOSCs-$EVs^{B16-BL6}$ were both co-internalized inside NIH-3T3 cells.

The cellular uptake of the EVs derived-membrane coated NPs was further quantified by flow cytometry analyses. In these experiments, cell cultures of B16-BL6 and NIH-3T3 were incubated separately with fluorescently-labelled ssOSCs-$EVs^{B16-BL6}$ (0.1 mg mL-1) and ssOSCs-$EVs^{NIH-3T3}$ (0.1 mg mL-1) for 2, 4, 8, 24 and 48 h. The single cell fluorescence emission intensity was measured and used as indicator of the amount of NPs internalized by each cell. As shown in Fig. 4C, the peak of fluoresce intensity shifted to a higher level when cell cultures were incubated with the NPs covered with their own EVs, suggesting the promoted NP internalization attributed to the EVs-associated membrane isolated from B16-BL6 melanoma cells. The internalization percentages are included in Table S2. The percentage of B16-BL6 cells that had taken up ssOSCs increased when they were covered with $EVs^{B16-BL6}$ compared to NPs coated with $EVs^{NIH-3T3}$. In the case of the healthy NIH-3T3 this tendency was less pronounced. Statistically significant differences in the percentage of cell internalization were obtained when compared B16-BL6 incubated with ssOSCs-$EVs^{B16-BL6}$ (64.3 % at 24 h and 65.1 % at 48 h) and ssOSCs-$EVs^{NIH-3T3}$ (45.5 % at 24 h and 45.2 % at 48 h). Even though we have used only the membranes of the EVs the results are in agreement with previous works, on the full exosomes, on the ability to target specific cells and to serve as selective vehicles for NPs delivery [61–63].

3.3. In vivo biodistribution and targeting properties of the EVs-NPs hybrids

Since the complexity of the tumor tissue and the crossing of the barriers, can cancel the selectivity *in vivo*, experiments were carried out to understand the biodistribution and targeting sites of ssOSCs-$EVs^{B16-BL6}$, as well as their potential *in vivo* antitumoral activity. We have performed the experiments in two different animal models: 1) subcutaneously transplanted murine B16-BL6 tumor; and 2) lung-metastasis after IV administration of B16-BL6. The first assessment included the biocompatibility and the biodistribution of ssOSCs-$EVs^{B16-BL6}$ and compared with the uncoated (naked) ssOSCs. Both naked and EVs-coated ssOSCs were fluorescently labelled with Cy5. To compare their biodistribution in mice, the labelling efficiency in terms of fluorescence at the injected dose (7 mgkg-1) was measured. Both formulations exhibited comparable emission intensity of the dye, allowing the comparison of fluorescence signals for both nanocarriers when using IVIS *in vivo* and *ex vivo* experiments (Fig. S8). *Ex vivo* analysis by IVIS, by

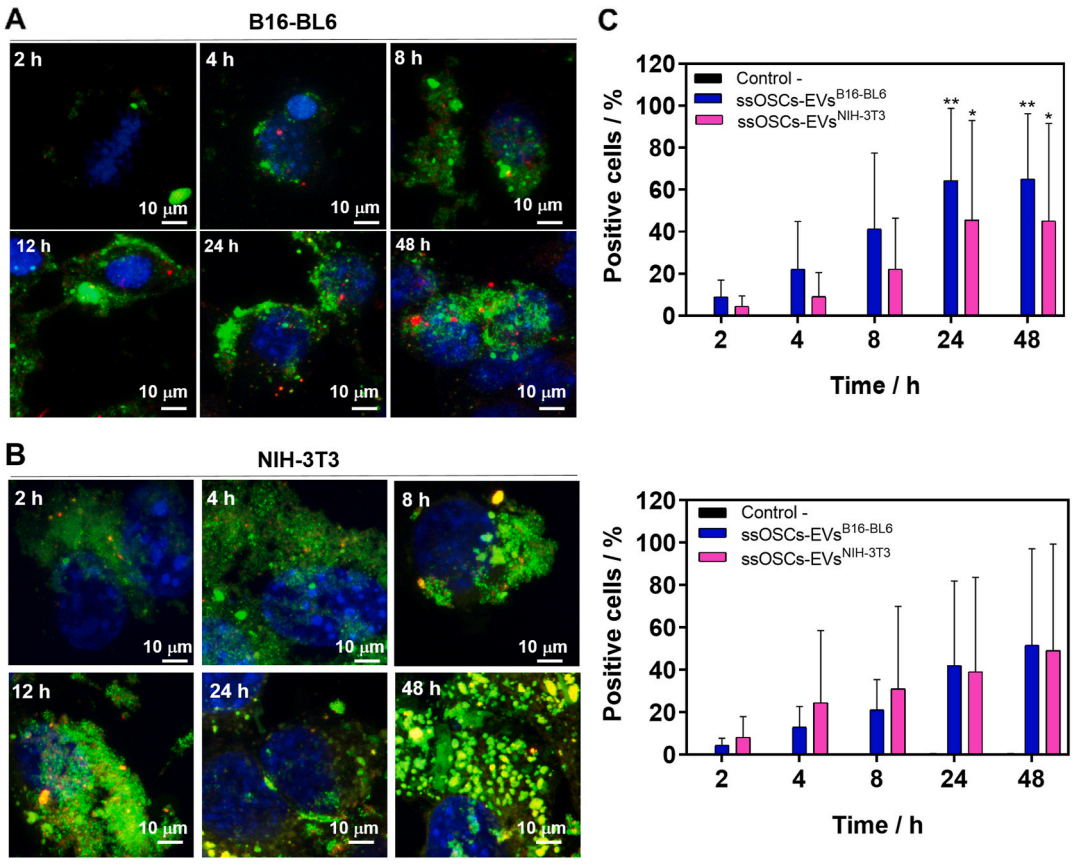

Fig. 4. *In vitro* internalization of ssOSCs-EVs$^{B16-BL6}$ and ssOSCs-EVs$^{NIH-3T3}$. A) Confocal microscopy of B16-BL6 co-incubated simultaneously with ssOSCs-EVs$^{B16-BL6}$ (in green) and ssOSCs-EVs$^{NIH-3T3}$ (in red). B) Confocal microscopy of NIH-3T3 cells co-incubated simultaneously with ssOSCs-EVs$^{B16-BL6}$ (in red) and ssOSCs-EVs$^{NIH-3T3}$ (in green). Nuclei are shown in blue. C) Flow cytometry analysis of B16-BL6 (upper panel) and NIH-3T3 cell (below panel) cultures incubated with ssOSCs-EVs$^{B16-BL6}$ or ssOSCs-EVs$^{NIH-3T3}$. Mean ± sd. *$p < 0.05$; **$p < 0.01$; ***$p < 0.0001$ y ****$p < 0.00001$. (For interpretation of the references to colour in this figure legend, the reader is referred to the Web version of this article.)

examining directly the organs of interest rather than the whole animal, reduces fluorescence disproportionalities of the organs located internally, and results in a higher sensitivity. To corroborate the fluorescence data ICP-OES was performed on each organ to determine the amount of silicium in the tissue.

Subcutaneous tumor model. An allograft model was implanted by subcutaneously injecting 2x10^5 B16-BL6 cells (see experimental section). Then, 100 μL of a PBS solution containing 7 mg kg-1 of ssOSCs or ssOSCs-EVs$^{B16-BL6}$ were administered in the tail vein and due to their fluorescence with the Cy5 dye attached to the silica core, their presence in the mice was visualized by IVIS as previously mentioned (see experimental part). The bioaccumulation of ssOSCs-EVs$^{B16-BL6}$ from *ex vivo* IVIS images and fluorescence intensity in the subcutaneous model is shown in Fig. 5A and B. The statistical analysis of these results was studied organ by organ, comparing the fluorescence level of the organs from mice treated with the ssOSCs-EVs$^{B16-BL6}$ and ssOSCs. The results show that ssOSCs were mainly accumulated in liver and spleen compared to the EV-coated ssOSCs, that were preferentially located in the lungs. In the case of pancreas and kidney, the accumulation of both NPs was similar and do not increase with time, suggesting that NPs accumulation in these organs was negligible. Also, no statistical significant differences were observed in the kidney. These data are in agreement with previously published works on the naked NPs that conclude that spleen and liver were the organs where more fluorescence signal with greater intensity was founded [47]. In the case of the subcutaneous tumor model, after 48 h a significant accumulation of EVs-coated ssOSCs was found in the tumor compared with the naked ssOSCs. The fluorescence of the different tissues was finally analyzed under microscope and after staining cell nuclei with DAPI (Fig. 5C and D).

As a more accurate alternative to fluorescence measurements and to corroborate lung targeting properties of ssOSCs-EVs$^{B16-BL6}$ we also measured the amount of silicium, coming from the silica NPs, in the different organs by ICP-OES after organ digestion (Fig. S9). In agreement with the fluorescence measurements, when administering ssOSCs-EVs$^{B16-BL6}$ most of the silicium was found in the lungs. The histopathological analysis performed in the HE stained sections of the animals treated with ssOSCs and ssOSCs-EVs$^{B16-BL6}$ did not reveal cellular morphological alterations that could be attributed to the accumulation of the NPs in any of the studied tissues when compared to control mice. In Figs. S10A and S10B, representative HE images of the studied organs from control and from ssOSCs and ssOSCs-EVs$^{B16-BL6}$ treated mice are shown at 4, 24, 48 h and 1 week after treatment. The presence of melanoma was observed in cutaneous samples. The examined organs, however, did not show the presence of metastasis. Regarding non-neoplastic features, the lungs showed some signs of slight atelectasis as seen in A −48h and -1st week, B −24h and −48h. Some spleen tissues had an expansion in their white pulp areas due to mild histiocytic infiltration. On the other hand, the organs such as pancreas, kidney and liver did not show a specific feature in both groups. It is interesting to note that macrophage proliferation or microvascular alterations were not observed.

Artificial metastasis model. For the artificial metastasis model, 5x10^4 B16-BL6_Luc cells were intravenously injected in the mice through the tail vein (see experimental section). Then, a PBS solution containing 7 mg kg-1 of ssOSCs or ssOSCs-EVs$^{B16-BL6}$ were administered and their biodistribution was analyzed in terms of fluorescence signal. The

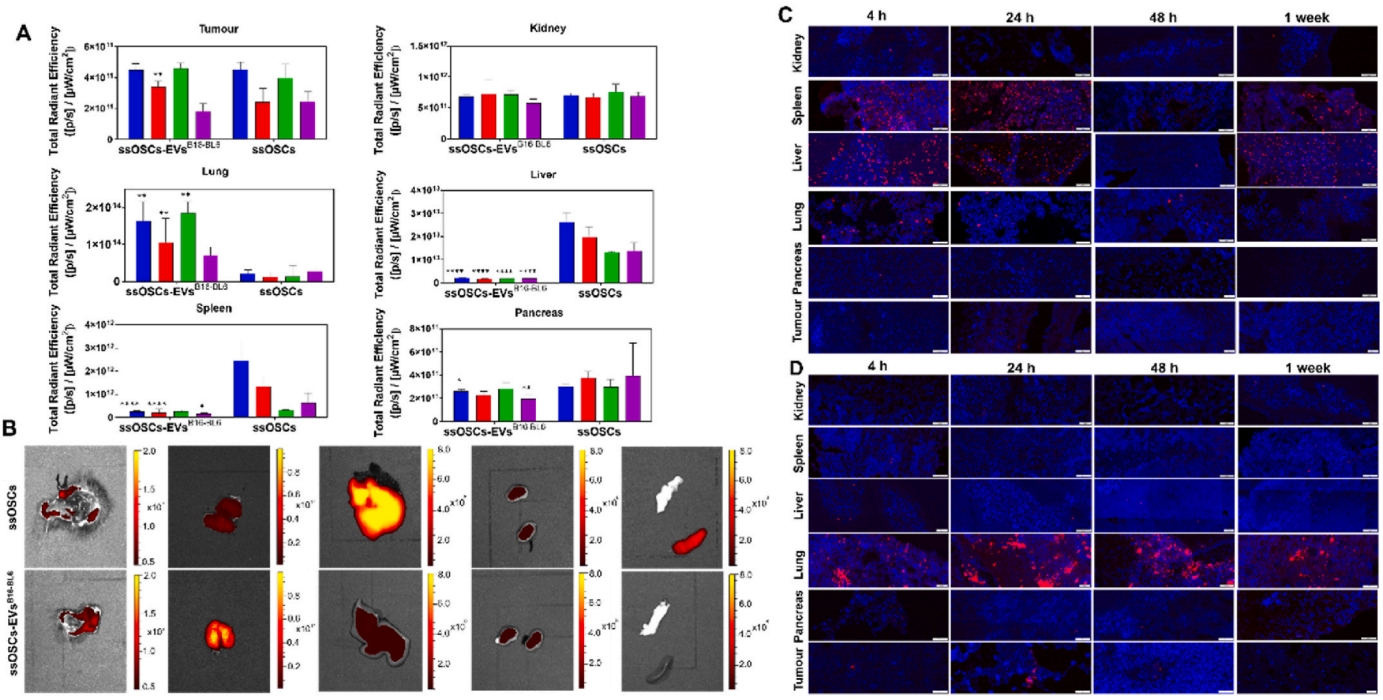

Fig. 5. A) Biodistribution of ssOSCs-EVs$^{B16-BL6}$ and ssOSCs in mice with the subcutaneous tumor model in terms of fluorescence quantified by IVIS. B) IVIS images of tumor, lung, liver, kidney, pancreas and spleen (from the left to the right) from a representative mouse for each group (n = 9) after 4 h of the vector administration. C) and D) Fluorescence microscopy images of immunofluorescence labelling of the tissues of mice with the subcutaneous tumor model treated with ssOSCs, and with ssOSCs-EVs$^{B16-BL6}$, respectively. The nuclei of the cells were marked with DAPI and appear in blue, while the fluorescent NPS are observed as red aggregates. Mean ± sd. *p < 0.05; **p < 0.01; ***p < 0.0001 and ****p < 0.00001. (For interpretation of the references to colour in this figure legend, the reader is referred to the Web version of this article.)

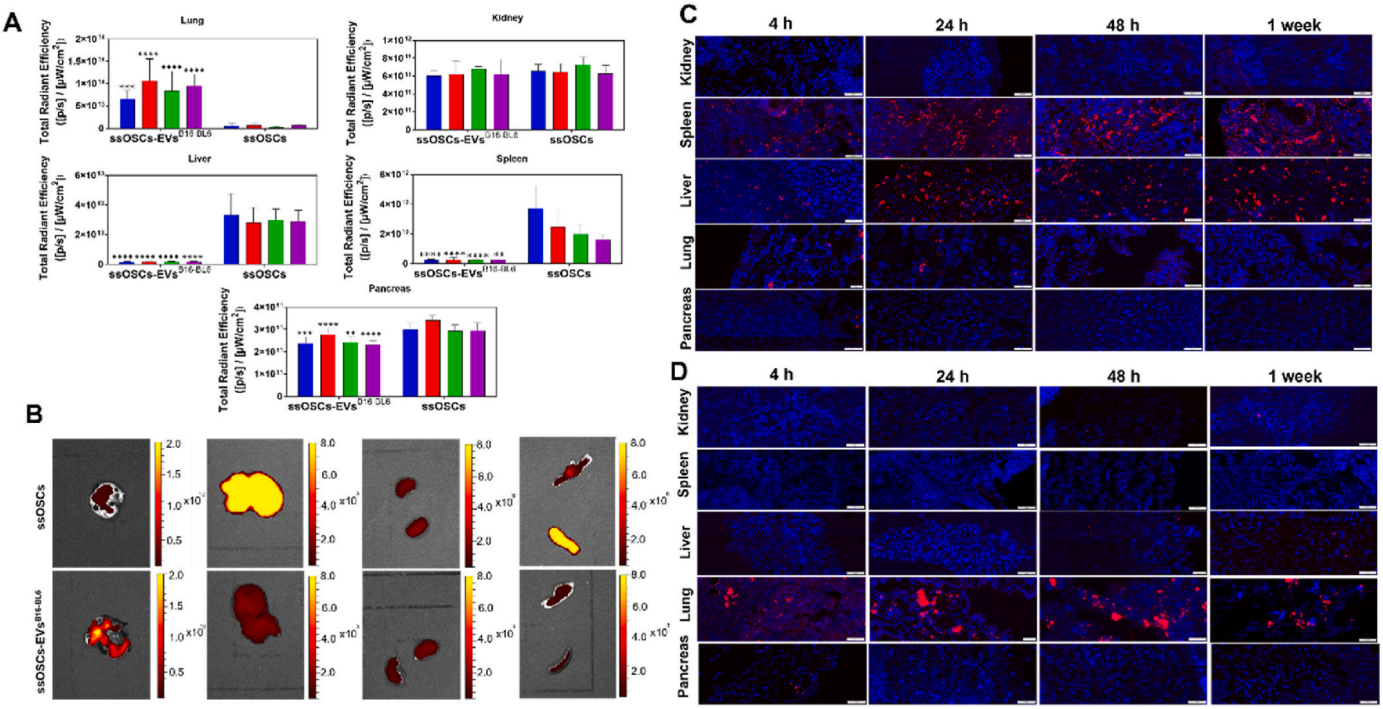

Fig. 6. A) Biodistribution of ssOSCs-EVs$^{B16-BL6}$ and ssOSCs in mice with the metastasis lung model in terms of fluorescence quantified by IVIS. B) IVIS images of lung, liver, kidney, pancreas and spleen (from the left to the right) from a representative mouse from each group (n = 9) after 4 h of the vector administration. C) Fluorescence microscopy images of immunofluorescence labelling of the tissues of mice with the metastasis model treated with ssOSCs. D) Fluorescence microscopy images of immunofluorescence labelling of the tissues of mice with the metastasis model treated with ssOSCs-EVs$^{B16-BL6}$. The nuclei of the cells were marked with DAPI and appear in blue, while the fluorescent NPS are observed as red aggregates. Mean ± sd. *p < 0.05; **p < 0.01; ***p < 0.0001 and ****p < 0.00001. (For interpretation of the references to colour in this figure legend, the reader is referred to the Web version of this article.)

biodistribution of ssOSCs and ssOSCs-EVs$^{B16-BL6}$ in the artificial metastatic model, was evaluated by IVIS fluorescence measurements (Fig. 6A–. B, Fig. 6C and D). Similar to the subcutaneous model, analysis of the fluorescence in the different organs indicated that most of the ssOSCS were accumulated in the liver and spleen. Interestingly, as in the previous model, the majority of the ssOSCs-EVs$^{B16-BL6}$ were located in the lungs. The quantification of Si (by ICP-OES) in the different organs at 4, 24, 48 h and 1 week after treatment confirmed IVIS fluorescence measurements (Fig. S11). The HE histopathological analyses of mice with the metastatic model did not revealed relevant histopathological changes in any of the organs analyzed potentially attributable to the presence of the NPs. Figure S12A and Figure S12B includes images of HE analysis in the metastatic mice model. Melanoma was observed in all subcutaneous samples as well as at least one metastatic focus in the lung samples. One mouse also presented metastasis in the peri-renal fat tissue as seen Figs. S11B–24h. On the other hand, many spleens showed a prominent expansion in the white pulps due to histiocytic infiltration while liver, pancreas and kidney samples did not show any significant pathological feature.

To corroborate that the accumulation of the ssOSCs-EVs$^{B16-BL6}$ was caused by the presence of the EVs membranes around the ssOSCs, a group of mice were treated with ssOSCs coated with liposomes (composed by cholesterol and phosphatidylcholine (PC)) with the same microviscosity and diameter of the ssOSCs-EVs$^{B16-BL6}$. Animal treated with control liposomes were sacrificed 48 h after their administration. Fig. S13 demonstrate that the liposomes-coated with ssOSCs exhibited the same biodistribution of naked ssOSCs, evidencing that the acting targeting against lungs of the ssOSCs-EVs$^{B16-BL6}$ was attributed to the presence of the EVs membranes.

The accumulation of the ssOSCs-EVs$^{B16-BL6}$ in the lungs is in agreement with previous works that affirm that EVs collected from B16-BL6 cells were delivered to the lungs [64]. In fact, it is well known the formation of lung metastasis after intravenous administration of B16-BL6 cells [65]. These results demonstrate that 1) EVs retain the specific lipids and membrane proteins of the source cells, thus maintaining the intrinsic targeting properties of parental cells [66,67]; and 2) by isolating B16-BL6 EVs derived-membranes and anchoring them electrostatically to ssOSCs, we have provided NPs with targeting properties towards lungs, similar to the natural EVs. Indeed even if lungs are usually filtering nanoparticles, they disappear from this organ in few hours [52]. For our nanoparticles, we have reported a highly visible signal of OSCs after 4 h of administration, and this signal decreased 3 order of magnitude during 24 h after treatment [47]. With the same nanoparticles, ssOSCs, covered with the EVs membranes derived from B16-BL6 remain through vessels without being entrapped and accumulated in non-desired tissues and are bioavailable at the target site organ.

3.4. Drug loading experiments

Encouraged by the *in vivo* targeting and as a proof of concept to evaluate the potential therapeutic properties of the ssOSCs-EVs$^{B16-BL6}$, the antitumoral standard drug, doxorubicin (DOX), was loaded inside the ssOSCs cavity before the EV membranes were assembled around them. DOX was encapsulated following a conventional impregnation protocol previously published [46]. The loaded ssOSCs were characterized by TEM, DLS, zeta potential and absorption spectroscopy (Fig. S14). Images indicate that NPs exhibited a uniform diameter distribution around 18 nm and DLS measurements revealed a hydrodynamic diameter around 20 nm (Figs. S14A and S14B). This size was in close agreement with values of empty NPs (Fig. 1A and B), indicating limited degree of aggregation of the NPs after drug encapsulation. Together with zeta potential (−11.61 mv), these results evidenced that DOX was located within the NPs core rather than being attached to their surface. Finally, we further demonstrated the encapsulation of the drug and its release from the NPs caused by the reduction of the disulfide bonds present in the silica framework. We conducted absorption spectroscopy experiments mimicking the physiological conditions in cancer cells, and in particular, the glutathione concentration (10 mM). The reduction of the disulfide bonds was addressed by incubating the NPs with glutathione 10 mM in PBS solution at a final concentration of 0.1 mg mL-1 during 24 h (37 °C, pH = 7.4). Finally, to determine the drug release, NPs were centrifuged and the absorption and emission spectra of the supernatant was measured to evaluate the loading of the DOX. ssOSCs incubated in the absence of GSH were used as negative control. Fig. S14C includes the emission spectra demonstrating how the emission intensity of the peak of DOX ($\lambda ex = 470$ nm) significantly increased in the presence of the GSH, evidencing the release of the drug after the reduction of the disulfide-responsive groups of the ssOSCs.

3.5. Application of the EVs-based vector as anticancer tools

The potential use of EVs-NPs hybrids as vectors for cancer treatment was tested in both *in vivo* tumor models. To this end, 7 mg kg-1 of DOX-loaded and, as control, empty EV-coated organosilica nanocages (ssOSCs@DOX-EVs$^{B16-BL6}$) were administered in the tail vein of the mice. Control groups included: mice treated with free DOX, mice treated with empty ssOSCs-EVs$^{B16-BL6}$ and untreated mice. Mice were treated three times with the vector corresponding to each group every 7 or 5 days in the case of the subcutaneous and metastatic models, respectively. The evolution of tumor growth was measured by a caliper (subcutaneous model) and by monitoring the bioluminescence intensity with IVIS (metastatic model). Also, in this tumor model, lung metastasis *ex vivo* were quantified and classified based on their number and dimensions at one ad interim (day 21) time point and at the end point of the experiment.

As indicated in Fig. 7A, tumor size of the three control groups increased progressively over time, being not responsive to DOX alone. In contrast, the tumor of mice treated with ssOSCs@DOX-EVs$^{B16-BL6}$ stopped growing after the first administration. A marginal effect, was observed with empty ssOSCs-EVs$^{B16-BL6}$, but for this group after an initial delay the tumor regrew. These results evidence that ssOSCs-EVs$^{B16-BL6}$ do not contribute to tumor progression or reduction. More importantly, we observe that ssOSCs@DOX-EVs$^{B16-BL6}$ can target the tumor and the encapsulated DOX preserves its antitumoral properties in the process of encapsulation and NPs covering with the EVs derived-membranes. Indeed, we have used as control the same amount of free DOX present in the ssOSCs@DOX-EVs$^{B16-BL6}$, but the efficacy in the tumor reduction is definitely higher when we can use a targeting nanocarrier vs the free drug.

In the case of the metastasis model, the tumor progression was analyzed by monitoring the bioluminescence of tumor cells by IVIS and by the actual count of lung metastasis. As expected, the expression of luciferase was detected in the lungs and, serve us to quantify the relative variations of the number of tumoral cells and their viability. Fig. 7B shows that, luciferase expression increases slower in the case of ssOSCs@DOX-EVs$^{B16-BL6}$ treated mice. These results were corroborated by metastasis quantification and at the end-point of the experiment (Fig. 7C). In mice receiving ssOSCs@DOX-EVs$^{B16-BL6}$ the number of metastasis lung colonies was significantly less than in the other groups. This difference was observed also in terms of tumor burden, where less metastases of bigger size (>2 mm) were observed, compared with the controls. As previously discussed, for ssOSCs@DOX-EVs$^{B16-BL6}$ treated mice, the hybrid nanocarrier tends to inhibit the formation of lung colonies of cancer cells that remained comparable to the ones detected at the baseline (day when treatment starts), indicating the ability of the drug to counteract metastasis. For ssOSCs@DOX-EVs$^{B16-BL6}$ treated mice showed a higher metastatic burden compared to baseline, although not significant, while the difference in metastasis >2 mm is observed between ssOSCs@DOX-EVs$^{B16-BL6}$ and controls (Fig. 7D). For ssOSCs@DOX-EVs$^{B16-BL6}$ treated mice, 36.6 % of animals exhibited comparable metastasis than the baseline, 36.6 % had a higher number of

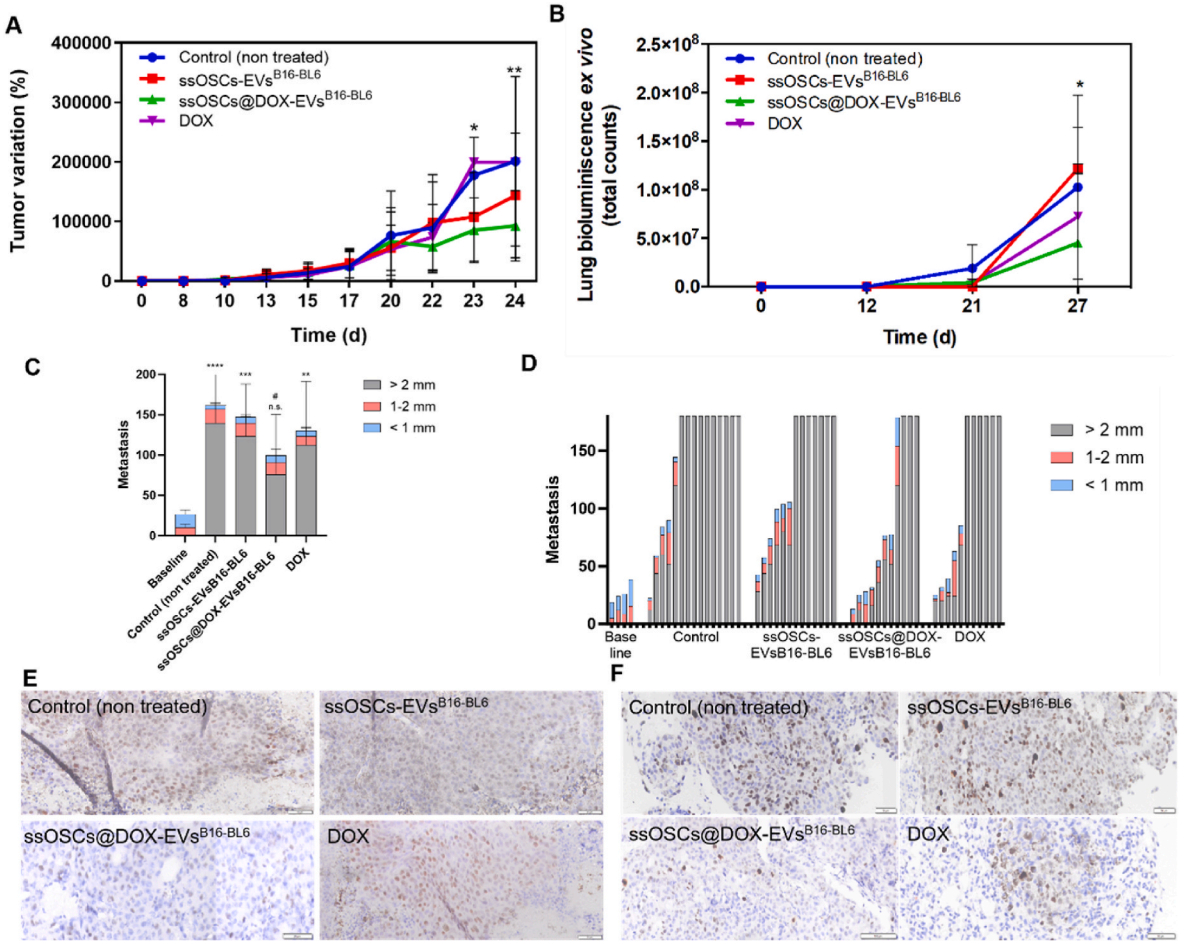

Fig. 7. A) Tumour variation (expressed in %) of B16-BL6 cells transplanted subcutaneously (n = 15 mice/group). Tumor-bearing mice were treated with vehicle, ssOSCs-EVsB16-BL6, DOX and ssOSCs@DOX-EVs$^{B16-BL6}$. B) Lungs bioluminescence of artificial metastasis tumor model quantified by IVIS. C) Number of metastasis in lungs. D) Metastatic burden, calculated by multiplying the number of metastasis by their volume. Columns are the number of metastasis, grouped by size, for each mouse/group. E) Ki-67 immunohistochemical staining of subcutaneous tumors. F) Ki-67 immunohistochemical staining of metastatic tumors. Ki-67 ratio was higher in control groups whereas a significant decrease of Ki-67 positive cells was observed for the ssOSCs-EVs$^{B16-BL6}$ treated mice in both cancer models. Mean ± sd. *p < 0.05; **p < 0.01; ***p < 0.0001 and ****p < 0.00001.

metastasis and 27 % presented lungs completed invaded of metastasis. On the contrary, the number of metastasis increased in control mice and in mice treated with ssOSCs-EVs$^{B16-BL6}$ or DOX alone (Fig. 7C). In fact, the 67 % of mice from the control group, the 54 % of animals treated with ssOSCs-EVs$^{B16-BL6}$ and the 55 % of DOX treated group, presented lungs completely invaded of metastasis.

To finally verify the antitumoral efficacy mediated by ssOSCs@DOX-EVs$^{B16-BL6}$, a histopathological analysis comparing control groups with the treatment group was carried out by Ki-67 staining. Ki-67 is a nuclear protein widely used as biomarker for cell proliferation and tumor progression (its expression in tumors in associated with cell proliferation and correlated with an increased growth rate and aggressiveness of cancer cells) [68]. The Ki-67 analysis indicated that in the case of the controls (non-treated) and the ssOSCs-EVs$^{B16-BL6}$-treated groups tumor cells in primary tumor and in metastasis were strongly positive, thus indicating their active proliferation status (Fig. 7E and F). On the contrary, DOX- and ssOSCs@DOX-EVs$^{B16-BL6}$-treated tumor cells of both cancer models exhibited a significantly low amount of positive signal. This decrease on Ki-67 expression was remarkably pronounced in the case of ssOSCs@DOX-EVs$^{B16-BL6}$ compared to the animals treated with the free drug. Thus, the decrease of Ki-67 expression signal in the treated groups of the subcutaneous tumor model and the metastasis-bearing mice is in agreement with the tumor growth observed. Fig. S15 includes the analysis of the percentage of Ki-67 positive tumor cells in both subcutaneous tumour and metastatic.

4. Conclusions

Herein we have created a multifunctional carrier based on EVs phospholipids/proteins membrane-coated breakable organo-silica nanocages containing DOX for targeted drug delivery. The advantage of this core-shell structured *vs* the more conventional lipid carriers is in the targeting functionalities intrinsic in the EVs membrane and in the much higher stability of the core that allow a better protection of the drug, prevent the leakage, enhance the intracellular accumulation and can be tailor made in shape and size. Also, this study proposes a completely new concept: the use of only the EVs membrane (where the targeting-responsive biomolecules of EVs are located) to avoid the main problem of EVs -based targeting, namely, that the contents from cancer cell-derived EVs may give rise to metastatic niches. The melanoma EVs isolated were emptied by a Folch method (avoiding the use of RNAs or other pro-oncogenetic EVs content), and reassembled on top of NPs, creating artificial EVs. We have demonstrated the preferential uptake *in vitro* (by confocal microscopy and flow cytometry) and the preferential accumulation, provided by the EVs membrane layer, of the vectors in tumors tissues in two different *in vivo* animal models. The targeting ability of the EVs-based organosilica NPs to the lungs was then exploited to reduce cancer growth and metastasis proliferation, using DOX, as a

drug, loaded in the nanocages. The biomimetic ssOSCs@DOX-EVs$^{B16-BL6}$ were able to penetrate into primary melanoma tumor and metastatic lesions of the lung greatly promoting the antiproliferation ability and the antitumoral efficacy of DOX compared to naked NPs. The efficacy of the ssOSCs@DOX-EVs$^{B16-BL6}$ in the two different animal models was demonstrated by the comparison with the empty carriers and free DOX. The design of the biomimetic delivery system herein proposed offers a novel approach to design EV-based delivery nanoplatforms with a high payload ability of antitumoral drugs and targeting moieties, thereby expanding their applicability for cancer theragnosis. The approach illustrated can be potentially exploited to treat not only cancer but also other respiratory or pulmonary diseases by using them as selective carriers for an efficient delivery of therapeutics.

CRediT authorship contribution statement

María Sancho-Albero: Writing – original draft, Funding acquisition, Data curation, Conceptualization. **Alessandra Decio:** Formal analysis, Data curation. **Reha Akpinar:** Formal analysis, Data curation. **Ada De Luigi:** Formal analysis, Data curation. **Raffaella Giavazzi:** Writing – review & editing. **Luigi M. Terracciano:** Writing – review & editing, Data curation. **Luisa De Cola:** Writing – original draft, Conceptualization, Funding acquisition.

Declaration of competing interest

The authors declare the following financial interests/personal relationships which may be considered as potential competing interests: Luisa De Cola reports financial support was provided by European Commission. Maria Sancho Albero reports financial support was provided by Italian Association for Cancer Research. If there are other authors, they declare that they have no known competing financial interests or personal relationships that could have appeared to influence the work reported in this paper.

Acknowledgements

This project has received funding from the European Union's Horizon 2020 research and innovation program under grant agreement no. 964386 (FET Open Mimic-Key project). M. S-A is thankful for the financial support from Mario Negri Young Investigator Grant ExAC project (8702) and support from FIRC-AIRC fellowship for Italy (26907-2021). We thank Mario Negri Institute for Pharmacological Research and Dr Victor Sebastián from the University of Zaragoza and ICTS LMA for the TEM images. We also thank the SAI "Servicio Análisis Químico" from the University of Zaragoza for the ICP-OES measurements to determine the Si content in mice organs.

Appendix A. Supplementary data

Supplementary data to this article can be found online at https://doi.org/10.1016/j.mtbio.2024.101433.

Data availability

Data will be made available on request.

References

[1] T. Lammers, Nanomedicine tumor targeting, Adv. Mater. 36 (26) (2024) 2312169, https://doi.org/10.1002/adma.202312169.
[2] J. Wu, The enhanced permeability and retention (EPR) effect: the significance of the concept and methods to enhance its application, J. Personalized Med. 11 (8) (2021), https://doi.org/10.3390/jpm11080771.
[3] A.K. Pearce, R.K. O'Reilly, Insights into active targeting of nanoparticles in drug delivery: advances in clinical studies and design considerations for cancer nanomedicine, Bioconjugate Chem. 30 (9) (2019) 2300–2311, https://doi.org/10.1021/acs.bioconjchem.9b00456.
[4] R Van Der Meel, E. Sulheim, Y. Shi, F. Kiessling, W.J.M. Mulder, Smart cancer nanomedicine, Nat. Nanotechnol. 14 (November) (2019) 1007–1017, https://doi.org/10.1038/s41565-019-0567-y.
[5] J. Shi, P.W. Kantoff, R. Wooster, O.C. Farokhzad, Cancer nanomedicine: progress , challenges and opportunities, Nat. Rev. Cancer 17 (2017) 20–37, https://doi.org/10.1038/nrc.2016.108.
[6] D. Mundekkad, W.C. Cho, Nanoparticles in clinical translation for cancer therapy, Int. J. Mol. Sci. 23 (3) (2022), https://doi.org/10.3390/ijms23031685.
[7] M.J. Mitchell, M.M. Billingsley, R.M. Haley, M.E. Wechsler, N.A. Peppas, R. Langer, Engineering precision nanoparticles for drug delivery, Nat. Rev. Drug Discov. 20 (2) (2021) 101–124, https://doi.org/10.1038/s41573-020-0090-8.
[8] Anarjan F. Salahpour, Active targeting drug delivery nanocarriers: ligands, Nano-Structures & Nano-Objects 19 (2019) 100370, https://doi.org/10.1016/j.nanoso.2019.100370.
[9] J. Shi, P.W. Kantoff, R. Wooster, O.C. Farokhzad, Cancer nanomedicine: progress, challenges and opportunities, Nat. Rev. Cancer 17 (1) (2017) 20–37, https://doi.org/10.1038/nrc.2016.108.
[10] T. Yang, J. Zhai, D. Hu, et al., "Targeting design" of nanoparticles in tumor therapy, Pharmaceutics 14 (9) (2022), https://doi.org/10.3390/pharmaceutics14091919.
[11] J. Yoo, C. Park, G. Yi, D. Lee, H. Koo, Active targeting strategies using biological ligands for nanoparticle drug delivery systems, Cancers 11 (640) (2019) 1–13.
[12] H. He, L. Liu, E.E. Morin, M. Liu, A. Schwendeman, Survey of clinical translation of cancer nanomedicines-lessons learned from successes and failures, Acc. Chem. Res. 52 (9) (2019) 2445–2461, https://doi.org/10.1021/acs.accounts.9b00228.
[13] W. Gao, C.M.J. Hu, R.H. Fang, L. Zhang, Liposome-like nanostructures for drug delivery, J. Mater. Chem. B 1 (48) (2013), https://doi.org/10.1039/C3TB21238F.
[14] M.D. Fulton, W. Najahi-Missaoui, Liposomes in cancer therapy: how did we start and where are we now, Int. J. Mol. Sci. 24 (7) (2023), https://doi.org/10.3390/ijms24076615.
[15] R. Tenchov, R. Bird, A.E. Curtze, Q. Zhou, Lipid Nanoparticles—From liposomes to mRNA vaccine delivery, a landscape of research diversity and advancement, ACS Nano 15 (11) (2021) 16982–17015, https://doi.org/10.1021/acsnano.1c04996.
[16] L. Maggini, I. Cabrera, A. Ruiz-Carretero, E.A. Prasetyanto, E. Robinet, L. De Cola, Breakable mesoporous silica nanoparticles for targeted drug delivery, Nanoscale 8 (13) (2016) 7240–7247, https://doi.org/10.1039/C5NR09112H.
[17] V. Cauda, A. Schlossbauer, T. Bein, Bio-degradation study of colloidal mesoporous silica nanoparticles: effect of surface functionalization with organo-silanes and poly(ethylene glycol), Microporous Mesoporous Mater. 132 (1) (2010) 60–71, https://doi.org/10.1016/j.micromeso.2009.11.015.
[18] E.J. Anglin, L. Cheng, W.R. Freeman, M.J. Sailor, Porous silicon in drug delivery devices and materials, Adv. Drug Deliv. Rev. 60 (11) (2008) 1266–1277, https://doi.org/10.1016/j.addr.2008.03.017.
[19] J.H. Park, L. Gu, G. von Maltzahn, E. Ruoslahti, S.N. Bhatia, M.J. Sailor, Biodegradable luminescent porous silicon nanoparticles for in vivo applications, Nat. Mater. 8 (4) (2009) 331–336, https://doi.org/10.1038/nmat2398.
[20] X. Xue, Y. Huang, R. Bo, et al., Trojan Horse nanotheranostics with dual transformability and multifunctionality for highly effective cancer treatment, Nat. Commun. 9 (1) (2018) 3653, https://doi.org/10.1038/s41467-018-06093-5.
[21] M.M. Encabo-berzosa, M. Gimeno, L. Lujan, et al., Selective delivery of photothermal nanoparticles to tumors using mesenchymal stem cells as Trojan horses, RSC Adv. 6 (2016) 58723–58732, https://doi.org/10.1039/C6RA10058A.
[22] M. Sancho-Albero, B. Rubio-ruiz, A.M. Pérez-lópez, et al., Cancer-derived exosomes loaded with ultrathin palladium nanosheets for targeted bioorthogonal catalysis, Nat. Catal. 2 (2019) 864–872.
[23] T. Yong, X. Zhang, N. Bie, et al., Tumor exosome-based nanoparticles are efficient drug carriers for chemotherapy, Nat. Commun. 10 (1) (2019) 3838, https://doi.org/10.1038/s41467-019-11718-4.
[24] X. Wang, L. Tian, J. Lu, I.O.L. Ng, Exosomes and cancer - diagnostic and prognostic biomarkers and therapeutic vehicle, Oncogenesis 11 (1) (2022) 54, https://doi.org/10.1038/s41389-022-00431-5.
[25] C. He, S. Zheng, Y. Luo, B. Wang, Exosome theranostics: biology and translational medicine, Theranostics 8 (1) (2018) 237–255, https://doi.org/10.7150/thno.21945.
[26] B. Thébaud, D.J. Stewart, Exosomes: cell garbage can, therapeutic carrier, or trojan horse? Circulation 126 (22) (2012) 2553–2555, https://doi.org/10.1161/CIRCULATIONAHA.112.146738.
[27] M. Yáñez-Mó, P.R.M. Siljander, Z. Andreu, et al., Biological properties of extracellular vesicles and their physiological functions, J. Extracell. Vesicles 1 (2015) 1–60.
[28] W. Niu, Q. Xiao, X. Wang, et al., A biomimetic drug delivery system by integrating grapefruit extracellular vesicles and doxorubicin-loaded heparin-based nanoparticles for glioma therapy, Nano Lett. 21 (3) (2021) 1484–1492, https://doi.org/10.1021/acs.nanolett.0c04753.
[29] J. Chen, J. Pan, S. Liu, et al., Fruit-derived extracellular-vesicle-engineered structural droplet drugs for enhanced glioblastoma chemotherapy, Adv. Mater. 35 (45) (2023) 2304187, https://doi.org/10.1002/adma.202304187.
[30] J. Li, X. Wang, H. Guo, et al., Immunostimulant citrus fruit-derived extracellular vesicle nanodrugs for malignant glioma immunochemotherapy, Chem. Eng. J. 484 (2024) 149463, https://doi.org/10.1016/j.cej.2024.149463.
[31] Q. Xiao, W. Zhao, C. Wu, et al., Lemon-derived extracellular vesicles nanodrugs enable to efficiently overcome cancer multidrug resistance by endocytosis-triggered energy dissipation and energy production reduction, Adv Sci (Weinheim, Baden-Wurttemberg, Ger. 9 (20) (2022) e2105274, https://doi.org/10.1002/advs.202105274.

[32] A. Hoshino, B. Costa-Silva, T.L. Shen, et al., Tumor exosome integrins determine organotripic metastasis, Nature 527 (7578) (2016) 329–335, https://doi.org/10.1038/nature15756.Tumour.
[33] J. Dai, Y. Su, S. Zhong, et al., Exosomes: key players in cancer and potential therapeutic strategy, Signal Transduct. Targeted Ther. 5 (1) (2020) 145, https://doi.org/10.1038/s41392-020-00261-0.
[34] D. Nie, Z. Dai, J. Li, et al., Cancer-cell-membrane-coated nanoparticles with a yolk–shell structure augment cancer chemotherapy, Nano Lett. 20 (2) (2020) 936–946, https://doi.org/10.1021/acs.nanolett.9b03817.
[35] Y. Zhao, Y. Zhu, K. Ding, S. Li, T. Liu, Biomimetic nanovesicle co-delivery system impairs energy metabolism for cancer treatment, J. Nanobiotechnol. 21 (1) (2023) 299, https://doi.org/10.1186/s12951-023-02061-4.
[36] A.J. Vázquez-Ríos, Á. Molina-Crespo, B.L. Bouzo, R. López-López, G. Moreno-Bueno, M. de la Fuente, Exosome-mimetic nanoplatforms for targeted cancer drug delivery, J. Nanobiotechnol. 17 (1) (2019) 85, https://doi.org/10.1186/s12951-019-0517-8.
[37] M. Lu, X. Zhao, H. Xing, et al., Comparison of exosome-mimicking liposomes with conventional liposomes for intracellular delivery of siRNA, Int. J. Pharm. 550 (1) (2018) 100–113, https://doi.org/10.1016/j.ijpharm.2018.08.040.
[38] G. Rosso, V. Cauda, Biomimicking extracellular vesicles with fully artificial ones: a rational design of EV-BIOMIMETICS toward effective theranostic tools in nanomedicine, ACS Biomater. Sci. Eng. 9 (11) (2023) 5924–5932.
[39] V.S. Chernyshev, D. Nozdriukhin, R. Chuprov-Netochin, et al., Engineered multicompartment vesicosomes for selective uptake by living cells, Colloids Surf. B Biointerfaces 220 (2022) 112953, https://doi.org/10.1016/j.colsurfb.2022.112953.
[40] X. Zhou, J. Mao, Y. Miao, et al., Tumour-derived extracellular vesicle membrane hybrid lipid nanovesicles enhance siRNA delivery by tumour-homing and intracellular freeway transportation, J. Extracell. Vesicles 11 (3) (2022) e12198, https://doi.org/10.1002/jev2.12198.
[41] Z. Wang, J. Rich, N. Hao, et al., Acoustofluidics for simultaneous nanoparticle-based drug loading and exosome encapsulation, Microsystems Nanoeng 8 (1) (2022) 45, https://doi.org/10.1038/s41378-022-00374-2.
[42] H. Li, S. Li, Y. Lin, et al., Artificial exosomes mediated spatiotemporal - resolved and targeted delivery of epigenetic inhibitors, J. Nanobiotechnol. 19 (2021) 1–16.
[43] J. Rezaie, M. Feghhi, T. Etemadi, A review on exosomes application in clinical trials: perspective, questions, and challenges, Cell Commun. Signal. 20 (1) (2022) 145, https://doi.org/10.1186/s12964-022-00959-4.
[44] L. Sun, R. Xu, X. Sun, et al., Safety evaluation of exosomes derived from human umbilical cord mesenchymal stromal cell, Cytotherapy 18 (3) (2016) 413–422, https://doi.org/10.1016/j.jcyt.2015.11.018.
[45] M. Sancho-Albero, G. Facchetti, N. Panini, et al., Enhancing Pt (IV) complexes anticancer activity upon encapsulation in stimuli responsive nanocages, Adv. Healthcare Mater. 12 (2023) 2202932, https://doi.org/10.1002/adhm.202202932.
[46] M. Sancho-Albero, G. Rosso, L. De Cola, V. Cauda, Cargo-loaded lipid-shielded breakable organosilica nanocages for enhanced drug delivery, Nanoscale 15 (35) (2023) 14628–14640, https://doi.org/10.1039/D3NR02155F.
[47] L. Talamini, P. Picchetti, L.M. Ferreira, et al., Organosilica cages target hepatic sinusoidal endothelial cells avoiding macrophage filtering, ACS Nano 15 (6) (2021) 9701–9716, https://doi.org/10.1021/acsnano.1c00316.
[48] K. Ma, Y. Gong, T. Aubert, et al., Self-assembly of highly symmetrical, ultrasmall inorganic cages directed by surfactant micelles, Nature 558 (7711) (2018) 577–580, https://doi.org/10.1038/s41586-018-0221-0.
[49] T. Aubert, J.Y. Huang, K. Ma, T. Hanrath, U. Wiesner, Porous cage-derived nanomaterial inks for direct and internal three-dimensional printing, Nat. Commun. 11 (1) (2020) 4695, https://doi.org/10.1038/s41467-020-18495-5.
[50] G. Poste, J. Doll, I.R. Hart, I.J. Fidler, In vitro selection of murine B16 melanoma variants with enhanced tissue-invasive properties, Cancer Res. 40 (5) (1980) 1636–1644.
[51] J.E. Talmadge, I.J. Fidler, AACR centennial series: the biology of cancer metastasis: historical perspective, Cancer Res. 70 (14) (2010) 5649–5669, https://doi.org/10.1158/0008-5472.CAN-10-1040.
[52] M. Sancho-Albero, M. Encinas-Giménez, V. Sebastián, et al., Transfer of photothermal nanoparticles using stem cell derived small extracellular vesicles for in vivo treatment of primary and multinodular tumours, J. Extracell. Vesicles 11 (3) (2022) e12193, https://doi.org/10.1002/jev2.12193.
[53] J. Folch, M. Lees, G.H. Sloane Stanley, A simple method for the isolation and purification of total lipides from animal tissues, J. Biol. Chem. 226 (1) (1957) 497–509.
[54] L. Diomede, S. Sozzani, W. Luini, et al., Activation effects of a prion protein fragment [PrP-(106-126)] on human leucocytes, Biochem. J. 320 (Pt 2) (1996) 563–570, https://doi.org/10.1042/bj3200563. Pt 2.
[55] S.D. Fowler, W.J. Brown, J. Warfel, P. Greenspan, Use of nile red for the rapid in situ quantitation of lipids on thin-layer chromatograms, J. Lipid Res. 28 (10) (1987) 1225–1232.
[56] I. Nakamura, S. Hama, S. Itakura, et al., Lipocalin2 as a plasma marker for tumors with hypoxic regions, Sci. Rep. 4 (1) (2014) 7235, https://doi.org/10.1038/srep07235.
[57] Z. Mousavikhamene, D.J. Sykora, M. Mrksich, N. Bagheri, Morphological features of single cells enable accurate automated classification of cancer from non-cancer cell lines, Sci. Rep. 11 (1) (2021) 24375, https://doi.org/10.1038/s41598-021-03813-8.
[58] M.A. Bonmati-Carrion, N. Alvarez-Sánchez, R. Hardeland, J.A. Madrid, M.A. Rol, A comparison of B16 melanoma cells and 3T3 fibroblasts concerning cell viability and ROS production in the presence of melatonin, tested over a wide range of concentrations, Int. J. Mol. Sci. 14 (2) (2013) 3901–3920, https://doi.org/10.3390/ijms14023901.
[59] M. Sancho-Albero, N. Navascués, G. Mendoza, V. Sebastián, M. Arruebo, Exosome origin determines cell targeting and the transfer of therapeutic nanoparticles towards target cells, J. Nanobiotechnol. 17 (16) (2019) 1–13, https://doi.org/10.1186/s12951-018-0437-z.
[60] T.A. Blumenfeld, H.S. Cheskin, M. Shinitzky, Microviscosity of amniotic fluid phospholipids, and its importance in determining fetal lung maturity, Clin. Chem. 25 (1) (1979) 64–67.
[61] R.N. Hamzah, K.M. Alghazali, A.S. Biris, R.J. Griffin, Exosome traceability and cell source dependence on composition and cell-cell cross talk, Int. J. Mol. Sci. 22 (10) (2021), https://doi.org/10.3390/ijms22105346.
[62] D.E. Murphy, O.G. de Jong, M. Brouwer, et al., Extracellular vesicle-based therapeutics: natural versus engineered targeting and trafficking, Exp. Mol. Med. 51 (3) (2019) 1–12, https://doi.org/10.1038/s12276-019-0223-5.
[63] P. Lara, A.B. Chan, L.J. Cruz, A.F.G. Quest, M.J. Kogan, Exploiting the natural properties of extracellular vesicles in targeted delivery towards specific cells and tissues, Pharmaceutics 12 (11) (2020), https://doi.org/10.3390/pharmaceutics12111022.
[64] T. Imai, Y. Takakura, Visualization and in vivo tracking of the exosomes of murine melanoma B16-BL6 cells in mice after intravenous injection, J. Biotechnol. 165 (2) (2013) 1–8, https://doi.org/10.1016/j.jbiotec.2013.03.013.
[65] K. Hyoudou, M. Nishikawa, Y. Umeyama, Y. Kobayashi, F. Yamashita, M. Hashida, Inhibition of metastatic tumor growth in mouse lung by repeated administration of polyethylene glycol-conjugated catalase: quantitative analysis with firefly luciferase-expressing melanoma cells, Clin. Cancer Res. 10 (22) (2004) 7685–7691, https://doi.org/10.1158/1078-0432.CCR-04-1020.
[66] S.C. Jang, Y.S. Gho, Could bioengineered exosome-mimetic nanovesicles be an efficient strategy for the delivery of chemotherapeutics? Nanomedicine (Lond). 9 (2) (2014) 177–180, https://doi.org/10.2217/nnm.13.206.
[67] B. Yang, Y. Chen, J. Shi, Exosome biochemistry and advanced nanotechnology for next-generation theranostic platforms, Adv. Mater. 31 (2) (2019) 1–33, https://doi.org/10.1002/adma.201802896.
[68] M. Maeyama, K. Tanaka, M. Nishihara, et al., Metabolic changes and anti-tumor effects of a ketogenic diet combined with anti-angiogenic therapy in a glioblastoma mouse model, Sci. Rep. 11 (1) (2021) 79, https://doi.org/10.1038/s41598-020-79465-x.